

Article

Efficient CsPbBr₃ Perovskite Solar Cells with Storage Stability > 340 Days

Shaochuan Hou, Siheng Wu, Xiaoyan Li, Jiahao Yan, Jie Xing, Hao Liu, Huiying Hao, Jingjing Dong * and Haichong Huang *

School of Science, China University of Geosciences, Beijing 100083, China

* Correspondence: jjdong@cugb.edu.cn (J.D.); hchhuang@cugb.edu.cn (H.H.)

Abstract: For CsPbBr₃ perovskite materials, it is especially important to reduce interface defects, suppress non-radiative recombination, and improve morphology to achieve highly efficient and stable CsPbBr₃ perovskite solar cells (PSCs). Herein, we reported a facile but highly efficient approach in additive engineering for improving the efficiency and stability of CsPbBr₃ PSCs. It was found that phenethylammonium iodide can passivate interface defects, suppress non-radiative recombination, and increase the grain sizes of CsPbBr₃ films by optimizing crystal quality and interface contact. As a result, a carbon-based CsPbBr₃ PSC with power conversion efficiency > 8.51%, storage stability > 340 days, and excellent harsh stability under high temperature and humidity, has been achieved.

Keywords: perovskite solar cells; CsPbBr₃; PEAI; in ambient air; stability



Citation: Hou, S.; Wu, S.; Li, X.; Yan, J.; Xing, J.; Liu, H.; Hao, H.; Dong, J.; Huang, H. Efficient CsPbBr₃ Perovskite Solar Cells with Storage Stability > 340 Days. *Energies* **2022**, *15*, 7740. <https://doi.org/10.3390/en15207740>

Received: 9 September 2022

Accepted: 13 October 2022

Published: 19 October 2022

Publisher's Note: MDPI stays neutral with regard to jurisdictional claims in published maps and institutional affiliations.



Copyright: © 2022 by the authors. Licensee MDPI, Basel, Switzerland. This article is an open access article distributed under the terms and conditions of the Creative Commons Attribution (CC BY) license (<https://creativecommons.org/licenses/by/4.0/>).

1. Introduction

Perovskite materials have shown enormous potential in photovoltaic power generation [1] due to their excellent characteristics, such as a tunable band gap, high light absorption coefficient, high carrier mobility, and weak exciton binding energy [2]. The power conversion efficiency (PCE) of perovskite solar cells (PSCs) has been improved from 3.8% to 25.7% in 11 years [3–5]. However, the long-term instability of organic–inorganic hybrid perovskite materials upon exposure to moisture, oxygen, and heat caused by organic cations [4] remains an issue. To improve the stability of perovskite materials, inorganic cesium ion (Cs⁺) was introduced to replace the organic counterparts to make all-inorganic perovskite materials, which was demonstrated to remarkably boost stability, especially in full-brominated CsPbBr₃ [6,7]. CsPbBr₃ was first applied into PSCs in 2015, presenting a PCE of 5.95% with outstanding moisture, oxygen, and thermal stability under harsh conditions [8]. Then, in 2016, Liu's group abandoned expensive Spiro-OMeTAD hole transport layers (HTL) and Au/Ag electrodes, designed the carbon-based CsPbBr₃ PSC, and obtained a PCE of 6.7% [8–12]. In 2018, Tang's group creatively put forward a multi-step spin-coating method to improve the crystal quality and morphology of the CsPbBr₃ active layers, resulting in a certified PCE of 9.72% [8–13]. Recently, the PCE of CsPbBr₃ PSCs was further increased to over 10% via a doping process, interface modification, or spectra engineering [8–12,14]. Although it improved rapidly, the performance of CsPbBr₃ PSCs is still unsatisfactory due to the wide band gap and severe carrier recombination of CsPbBr₃ films, which will cause a decline in PCE and stability [10]. Furthermore, the wide band gap of CsPbBr₃ leads to a large optical absorption loss, which significantly hinders further PCE improvements of CsPbBr₃ PSCs [3,12]. A widely reported solution to this impasse is partially substituting Br[−] with I[−] to reduce the band gap; however, the long-term stability declines significantly after the substitution [12,15,16]. So, long-term stability is still a problem for CsPbBr₃ PSCs when widening optical absorption [11,15,17–19]. Regarding the severe carrier recombination in CsPbBr₃ PSCs, a mass of defects at the interface and grain boundaries usually acts as non-radiative recombination centers. Furthermore, different

from organic–inorganic hybrid perovskite materials, a higher annealing temperature over 200 °C is necessary for CsPbBr₃ films, which leads to a rapid growth of crystals, resulting in a poor crystal quality with lots of defects, uneven grain size, and large traps. Thus, for the CsPbBr₃ perovskite materials, it is especially important to reduce interface defects, suppress non-radiative recombination, and improve morphology to achieve highly efficient CsPbBr₃ PSCs [11,20]. Recently, it has been widely reported that phenethylammonium iodide (PEAI) can passivate interface defects, suppress non-radiative recombination [21,22], and increase the grain sizes of organic–inorganic hybrid perovskites by doping into the precursor solution [23]. However, the application of PEAi in the synthesis of CsPbBr₃ perovskite film has never reported.

Herein, CsPbBr₃ films were synthesized by a multi-step spin-coating method, and PEAi was introduced into the CsPbBr₃ films for the first time via doping into the PbBr₂ precursor solution. It was found that PEAi can passivate interface defects, suppress non-radiative recombination, and increase the grain sizes of CsPbBr₃ films by optimizing crystal quality and interface contact. As a result, a carbon-based CsPbBr₃ PSC with a PCE > 8.51%, storage stability > 340 days, and excellent harsh stability under high temperature and humidity has been achieved. The whole preparation process of CsPbBr₃ PSCs was carried out in ambient air without humidity control.

2. Materials and Methods

We performed all experiments with the air at room temperature without humidity and temperature control.

2.1. Substrate and Precursor Solutions Preparation

We cleaned the dioxide transparent conductive glass doped with fluoride (FTO) by ultrasonic successively dipped in acetone, isopropanol, ethanol, deionized water, and isopropanol for 15 min. Then, we cleaned the FTO substrates by plasma. After that, we deposited the compact TiO₂ (c-TiO₂) from a solution of titanium tetraisopropoxide and hydrochloric acid in anhydrous ethanol by spin-coating at 3000 rpm for 30 s. We annealed the c-TiO₂ layer at 500 °C for 30 min. We diluted mesoporous TiO₂-layer (m-TiO₂) pastes (30 NR-D, Dyesol) in ethanol (1:4, weight ratio), then spin-coated at 5000 rpm for 45 s, and finally annealed at 500 °C for 30 min, as described in our previous article [24]. We prepared the PbBr₂ precursor solution by dissolving 367 mg PbBr₂ in 1 mL N,N-Dimethylformamide (DMF) under active stirring for 12 h. We doped the PbBr₂ precursor solutions of the experimental groups by PEAi at concentrations of 5, 10, and 15 mg/mL.

2.2. Multi-Step Spin-Coating Process of CsPbBr₃ Films

The multi-step spin-coating process of CsPbBr₃ films is illustrated in Figure S1 in the Supplementary Materials. We placed the FTO/c-TiO₂/m-TiO₂ substrates and the prepared PbBr₂ precursor solution on a 90 °C hot plate to preheat. We spin-coated the PbBr₂ solution on the substrates at a speed of 2000 rpm for 30 s. We placed the substrates with the spin-coated PbBr₂ solution on a hot plate at 90 °C and annealed for 30 min. Subsequently, we spin-coated the 0.07 M CsBr solution on the PbBr₂ layers 5 times. Each time, we annealed those substrates on a hot plate at 250 °C for 5 min, which was also reported in our previous article [25].

2.3. Device Fabrication

We scrapped the carbon electrode on the active layers. The area of each battery electrode is 0.01 cm². We obtained the solar cell devices after annealing 120 °C for 15 min. Schematic structure of the carbon-based mesoscopic PSC is shown in Figure 1a.

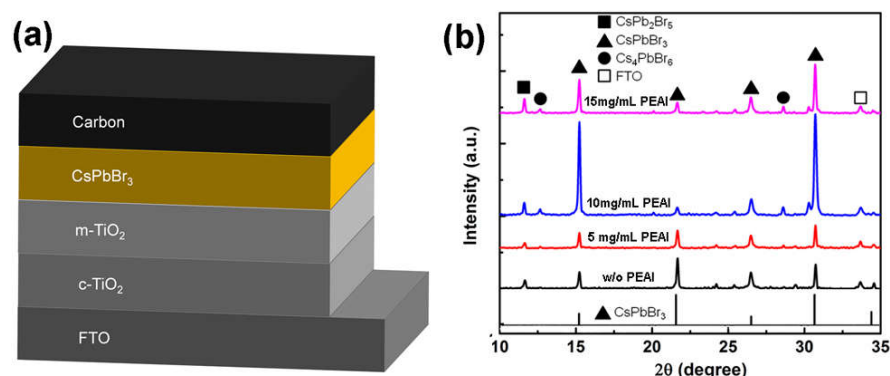


Figure 1. (a) Schematic structure of CsPbBr₃ PSCs; (b) XRD patterns of CsPbBr₃ films without and with PEAI doping in different concentrations.

2.4. Characterization

We characterized the surface morphology of perovskite films by scanning electron microscope (SEM). We tested the structure and components by X-ray diffraction technique (XRD, D8 fucox) and X-ray photoelectron spectroscopy (XPS). We determined the light absorbance spectra by UV–vis absorption spectra. We conducted Photoluminescence (PL) and time-resolved photoluminescence (TRPL) spectra to characterize the carrier transport properties. We measured dark J–V and space-charge limited-current (SCLC) curves to analyze defect-related information. We conducted current density–voltage (J–V) and monochromatic incident photon-to-electron conversion efficiency (EQE) experiments to characterize the performance of PSCs.

3. Results and Discussion

XRD spectra of CsPbBr₃ films without and with PEAI doping in different concentration have been performed as shown in Figure 1b. The optical setup and scan parameters of XRD scans for all the four samples are unified. Three characteristic peaks centered at around 15.2°, 21.7°, 26.5°, and 30.8° correspond to (100), (110), (111), and (200) planes of CsPbBr₃ phase, respectively. Obviously, all the four spectra exhibit almost identical peak positions, indicating the introduction of PEAI does not change the crystal structure and lattice constant of CsPbBr₃ films. However, the (100) and (200) diffraction peaks of CsPbBr₃ phase are dramatically enhanced after doping PEAI at 10 mg/mL. This is clear evidence for the optimization of crystallinity by PEAI doping at 10 mg/mL [14,26]. Furthermore, the appearance of the characteristic peaks of CsPb₂Br₅ and Cs₄PbBr₆ phases demonstrates that there are residuals of PbBr and CsBr in the four CsPbBr₃ films.

SEM has been introduced to characterize the surface morphology of CsPbBr₃ films. Figure 2a–d show top-view SEM images of CsPbBr₃ films undoped and doped with PEAI at 5, 10, and 15 mg/mL. We observed that the grain sizes of the undoped CsPbBr₃ film are small, and they increase with the further concentration of the PEAI additive. The grain sizes of the CsPbBr₃ films are undoped and doped with PEAI at 5, 10, and 15 mg/mL are 0.45, 0.67, 1.11, and 1.13 μm, respectively, which are obtained by the “Nanomeasurer” software. It is reported that most of these small crystal grains in the undoped CsPbBr₃ film are the phase of CsPb₂Br₅, which agrees with our previous XRD results [1]. The introduction of PEAI affects the kinetics of the crystallization process of CsPbBr₃ films, inhibits the formation of CsPb₂Br₅, and finally increases the grain size [9]. In addition, for PEAI-doped CsPbBr₃ films, it is obvious that two-dimensional (2D) perovskite material has formed at the grain boundaries, which is reported to generate in the crystallization process of CsPbBr₃ and could passivate interface defects at the grain boundaries [26]. The formation of 2D perovskite material caused by the addition of PEAI is not significantly visible when the concentration of PEAI is low, such as at 5 mg/mL, as shown in Figure 2b. However, by adding an excessive amount of PEAI, the 2D perovskite material is clearly observable, as presented in Figure 2d. Figure 2e,f present the cross-sectional morphological

properties of CsPbBr₃ films undoped and doped with PEAI at 10 mg/mL, respectively. The thickness of the CsPbBr₃ film after PEAI doping is ~650 nm, the same as the undoped film. We can see that the undoped CsPbBr₃ film exhibits an uneven surface and obvious pinholes. The extrusion of the grains against each other results in partial convex grains, leaving notable pinholes between the substrate and CsPbBr₃ film. On the contrary, the PEAI-doped CsPbBr₃ film presents uniform and full coverage. The increased grain size, reduced interface defects, and uniform and full coverage of PEAI-doped CsPbBr₃ films will promote light capture and charge transportation.

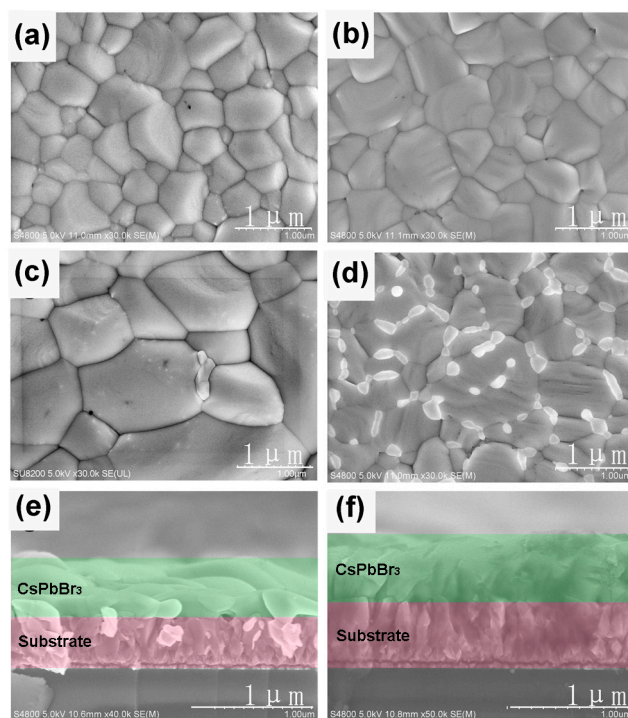


Figure 2. Top-view SEM images of CsPbBr₃ films (a) undoped and doped with PEAI at (b) 5, (c) 10, and (d) 15 mg/mL. Cross-sectional SEM images of CsPbBr₃ films (e) undoped and (f) doped with 10 mg/mL PEAI.

Combined XRD and SEM results confirm that the optimal doping concentration of PEAI is 10 mg/mL; therefore, CsPbBr₃ films doped with PEAI at 10 mg/mL were used for the following film characterization and PSC application.

To further verify the elemental composition and chemical structure of the CsPbBr₃ films without and with PEAI doping, XPS has been performed. Figure 3a–c are the high-resolution XPS spectra of Cs 3d, Pb 4f, and Br 3d, respectively. We can see that Pb and Br peaks shift to higher binding energies upon doping PEAI into CsPbBr₃ films, while peaks of Cs 3d_{3/2} and Cs 3d_{5/2} present nearly no variations. It is known that large-radius PEA⁺ cations play a supporting role in the perovskite crystallization process and promote the oriented growth of PEAI-doped CsPbBr₃ films [6,14], leading to the formation of 2D perovskite material, which may cause the distortion of the PbBr₆ octahedron and then increase the electron density of Pb and Br atoms. Therefore, for PEAI-doped CsPbBr₃ film, the XPS spectra of Pb 4f and Br 3d present blue shifts. In addition, based on the Pb 4f and Br 3d nuclear-energy-level spectra in Figure 3d, the Pb:X (X = Br) ratio of the undoped CsPbBr₃ film can be estimated to be 1:1.665 (calculated by Avantage software), indicating that there is a serious lack of Br on the surface, which may lead to obvious point defects. After the introduction of PEAI, the Pb:X (X = Br, I) ratio increased to 1:1.689, demonstrating that the point defects on the perovskite surface have been partially passivated and the Br vacancies are likely to be filled by a small amount of I[−] in PEAI [24].

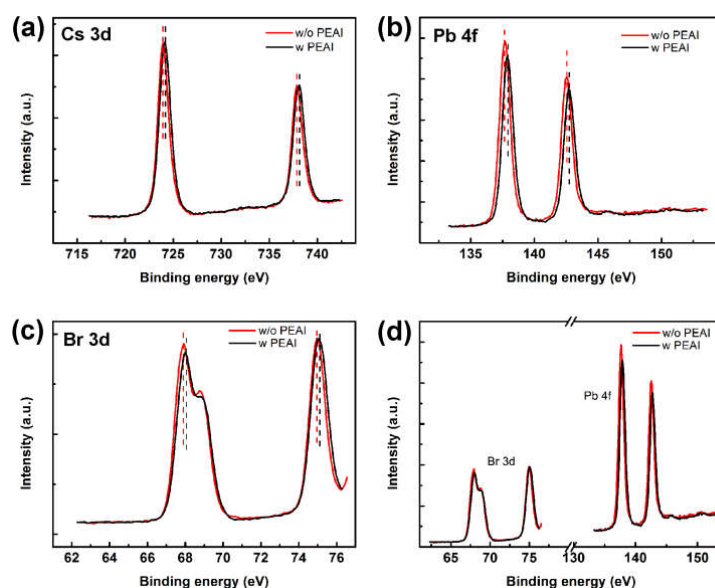


Figure 3. High-resolution XPS spectra of (a) Cs 3d, (b) Pb 4f, and (c) Br 3d. Pb 4f and Br 3d core-energy-level spectra are compared in (d).

UV-vis absorbance spectra have been carried out, and the results are shown in Figure 4a. Obviously, there is no change in the absorption edge of both perovskite films, indicating that the PEAI doping does not affect the band gap of CsPbBr₃ films [2,27]. In addition, a slight increase in the optical absorption is observed for the PEAI-doped CsPbBr₃ film, as shown in Figure 4a, which can be explained as follows: the uniform and full coverage of PEAI-doped CsPbBr₃ film will promote light capture and lead to improved optical absorption. Steady PL and TRPL measurements are presented in Figure 4a,b, respectively. Here, the samples used for steady PL and TRPL tests are CsPbBr₃ films directly deposited on the Al₂O₃ substrates without an electron transport layer (ETL) or HTL. As a result, light-induced carriers in an excited state cannot be extracted quickly, leading to radiation recombination. Here, higher steady PL intensity and slower TRPL decay rates demonstrate fewer traps or defects. We can see that the steady PL spectra of CsPbBr₃ films undoped and doped with PEAI exhibit an identical peak centered at about 532 nm, demonstrating that the PEAI doping does not affect the crystal structure of CsPbBr₃ films, which fully agrees with the UV-vis results. In addition, the PEAI-doped perovskite film exhibits a remarkably enhanced PL intensity compared with the undoped film, implying that the trap and defect states in CsPbBr₃ films are reduced. The TRPL spectra in Figure 4b can be well fitted by a bi-exponential decay function [11,22], and the corresponding lifetimes τ_1 , τ_2 , and τ_{ave} are obtained. After PEAI treatment, both τ_1 , τ_2 , and τ_{ave} increase greatly, from 15.12, 539.87, and 514.68 ns to 61.54, 700.80, and 635.60 ns, respectively, which can be attributed to the suppression of defect-related non-radiative recombination after PEAI doping, which is consistent with the steady PL results.

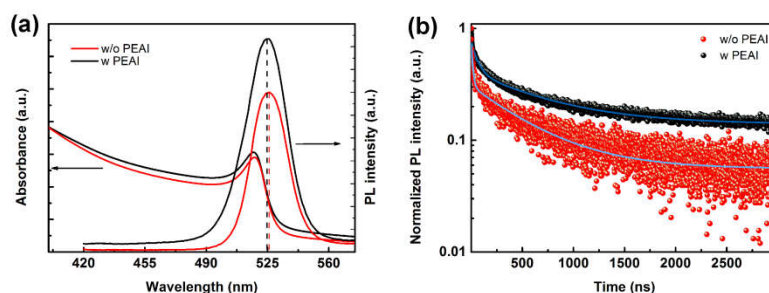


Figure 4. (a) UV-vis absorbance, steady PL, and (b) TRPL spectra of CsPbBr₃ films undoped and doped with 10 mg/mL PEAI without ETL or HTL.

The dark J–V measurements have been conducted with the architecture of FTO/*c*-TiO₂/*m*-TiO₂/CsPbBr₃/carbon, and the corresponding results are shown in Figure 5. It can be seen from Figure 5a that the dark current of the PEAI-doped device is about two orders of magnitude lower than the undoped device, implying reduced charge carrier recombination losses, which can be due to the reduced interface defects in the CsPbBr₃ layer after PEAI doping, as shown in previous SEM and XPS results [20,28]. The SCLC curves, which were measured with FTO/CsPbBr₃/Au architectures under dark conditions, are displayed in Figure 5b. The onset voltage of the trap-filled limit (V_{TFL}) can be obtained from the SCLC curves, and then we can calculate the trap state density (N_t) according to the following equation [6]:

$$N_t = \frac{2\epsilon_r\epsilon_0 V_{TFL}}{qL^2} \quad (1)$$

In this equation, L is the thickness of perovskite films, ϵ_r is the relative dielectric constant for CsPbBr₃, and ϵ_0 is the vacuum permittivity. From the SCLC curves in Figure 5b, the V_{TFL} of the undoped and PEAI-doped CsPbBr₃ layers are 1.0727 and 0.7915 V, respectively. Combined with Formula (1), the N_t of the undoped and PEAI-doped CsPbBr₃ layers are calculated to be 9.907×10^{15} and $7.310 \times 10^{15} \text{ cm}^{-3}$, respectively. It can be inferred that the trap states that lead to carrier recombination are significantly reduced after PEAI treatment, cross-checking the above-mentioned conclusion [6].

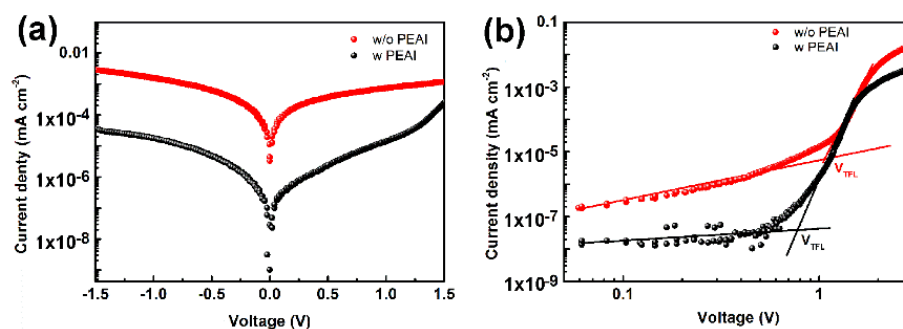


Figure 5. (a) Dark J–V and (b) SCLC versus voltage curves of undoped and PEAI-doped devices (V_{TFL} are obtained to be 1.061 and 0.776 V for the undoped and PEAI-doped devices, respectively).

A series of CsPbBr₃ PSCs are fabricated with an architecture of FTO/compact-TiO₂/mesoporous-TiO₂/CsPbBr₃/carbon. The active area is 0.1 cm², and the whole preparation process of the PSCs was finished in ambient air. The dependences of photovoltaic performances on PEAI concentrations are reflected by Figure S2 in the Supplementary Materials, and the corresponding photovoltaic parameters are summarized in the inset of Figure S2, which shows that the optimal doping concentration of PEAI is 10 mg/mL, consistent with the XRD and SEM characterization above.

Figure 6a shows the characteristic J–V curves of PSCs based on CsPbBr₃ films without and with PEAI doping at 10 mg/mL, and the corresponding photovoltaic parameters, short-circuit current density (J_{SC}), open-circuit voltage (V_{OC}), fill factor (FF), and PCE are summarized in the inset of Figure 6a. Obviously, the photoelectric conversion capability of devices has been tremendously improved upon PEAI doping, yielding a champion PCE of 8.51%. Specifically, V_{OC} rises from 1.28 V to 1.39 V, J_{SC} from 7.49 mA/cm² to 8.22 mA/cm², FF from 68% to 74%, and the PCE is enhanced by 26.87% compared with 6.55% for the undoped device. All the photovoltaic parameters increase notably, indicating that the total series resistance of the entire device is reduced by PEAI doping, which can be attributed to the reduced traps and defects, as confirmed above. From Figure 6a, we also noticed that a smaller J–V hysteresis can be achieved in the PEAI-doped PSC under forward and reverse scan directions. The hysteresis index [29], which is the ratio of PCE under reverse and forward scan, is decreased from 1.21 to 1.11 after PEAI doping, implying the passivation of interface defects in the PEAI-doped CsPbBr₃ layer. It was reported that ion migration

tended to occur at the defects/grain boundary in the active layer, which leads to J–V hysteresis [23,27]. The IPCE spectrum of the champion device is shown in Figure 6b, from which the integrated current density is calculated to be 7.68 mA/cm², agreeing well with the J–V result and confirming the accuracy of our measurement.

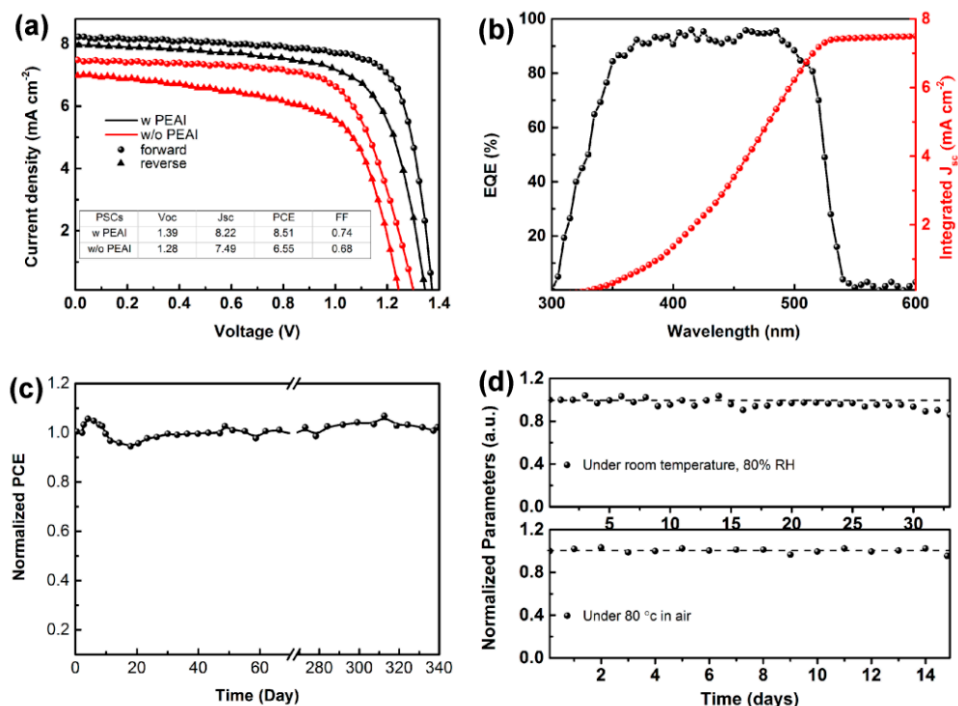


Figure 6. Characteristic J–V curves of PSCs based on CsPbBr₃ films without and with PEAI doping at 10 mg/mL, and (a) the inset shows corresponding photovoltaic parameters; (b) PCE spectrum of the champion device; (c) storage stability in the ambient air without encapsulation; (d) stability under harsh conditions.

As known, improving cell efficiency and reducing costs without sacrificing long-term stability are necessary for future commercial applications [12]. To study the storage stability, the PSC doped with PEAI at 10 mg/mL stored in ambient air (temperature: 10–20 °C, relative humidity: 20–30%) without encapsulation was measured. As shown in Figure 6c, for the device doped with PEAI, the PCE not only did not decline but increased after a few months of storage. According to reports, the PCE enhancement of CsPbBr₃ solar cells after storage may be attributed to the improved crystal quality of CsPbBr₃ film under the effect of water molecules. Furthermore, it should be noted that the efficiency of PEAI-doped PSC remained nearly unchanged for more than 11 months (340 days). For comparison, the storage stability of the non-doped PSC was measured under the same conditions and shown in Figure S3 in the Supplementary Materials. Obviously, the storage stability is remarkably improved after PEAI doping. In addition to storage stability in ambient air, stability under harsh conditions, such as high humidity and temperature, was also tested, as shown in Figure 6d. We can see that the PCE of PEAI-doped PSCs has almost no reduction under 80% humidity or at 80 °C without encapsulation within 30 or 14 days, while the devices without PEAI doping declined rapidly. The improvement of device stability after PEAI doping could also be attributed to the reduced traps and defects, which can lead to the suppression of charge recombination and accumulation.

4. Conclusions

In conclusion, to reduce interface defects, suppress non-radiative recombination, and improve the morphology of the CsPbBr₃ films to achieve highly efficient and stable CsPbBr₃ PSCs, we reported a facile but highly efficient approach for additive engineering. CsPbBr₃ films were synthesized by a multi-step spin-coating method, and PEAI was introduced into the CsPbBr₃ films for the first time via doping into the PbBr₂ precursor solution. We found that PEAI additive can passivate interface defects, suppress non-radiative recombination, and increase the grain sizes of CsPbBr₃ films by optimizing crystal quality and interface contact. By virtue of PEAI doping, a carbon-based CsPbBr₃ PSC with a PCE > 8.51%, storage stability > 340 days, and excellent stability under high temperature and humidity, has been achieved. Our work contributes to improving the performance of CsPbBr₃ PSCs.

Supplementary Materials: The supporting information can be downloaded at: <https://www.mdpi.com/article/10.3390/en15207740/s1>, Figure S1: Schematic diagram of multi-step spin-coating process to prepare CsPbBr₃ films; Figure S2: J–V characteristics of various CsPbBr₃ PSCs under illumination (AM 1.5 G, 100 mW cm^{−2}) undoped and doped with 5, 10 and 15 mg/mL PEAI, measured at the maximum power point; Figure S3: Storage stability (in the ambient air, without encapsulation) of CsPbBr₃ PSCs without PEAI-doping; Figure S4: J–V characteristics and storage stability (in the ambient air, without encapsulation) of CsPbBr₃ PSCs with different electrode.

Author Contributions: Conceptualization, S.H. and S.W.; methodology, X.L.; software, J.X.; validation, S.H., S.W. and X.L.; formal analysis, S.H.; investigation, H.H. (Haochong Huang); resources, J.D.; data curation, J.Y.; writing—original draft preparation, S.H.; writing—review and editing, S.W.; visualization, H.L.; supervision, H.H. (Huiying Hao); project administration, J.D.; funding acquisition, J.D. All authors have read and agreed to the published version of the manuscript.

Funding: This work was supported by the “Fundamental Research Funds for the Central Universities” (Grant No. 2652019121) and “the National Natural Science Foundation of China” (Grant No. 11404293).

Institutional Review Board Statement: Not applicable.

Informed Consent Statement: Not applicable.

Data Availability Statement: Not applicable.

Conflicts of Interest: The authors declare no conflict of interest.

References

1. Zhao, F.; Guo, Y.; Wang, X.; Tao, J.; Li, Z.; Zheng, D.; Jiang, J.; Hu, Z.; Chu, J. Efficient carbon-based planar CsPbBr₃ perovskite solar cells with Li-doped amorphous Nb₂O₅ layer. *J. Alloy. Compd.* **2020**, *842*, 1559840. [[CrossRef](#)]
2. Xu, W.; Gao, Y.; Ming, W.; He, F.; Li, J.; Zhu, X.; Kang, F.; Li, J.; Wei, G. Suppressing Defects-Induced Nonradiative Recombination for Efficient Perovskite Solar Cells through Green Antisolvent Engineering. *Adv. Mater.* **2020**, *32*, 1–10. [[CrossRef](#)] [[PubMed](#)]
3. Miyasaka, T.; Kulkarni, A.; Kim, G.M.; Öz, S.; Jena, A. Perovskite Solar Cells: Can We Go Organic-Free, Lead-Free, and Dopant-Free? *Adv. Energy Mater.* **2019**, *10*, 1–20. [[CrossRef](#)]
4. Wang, Y.; Hu, Z.; Yao, W.; Yang, C.; Zhang, H.; Zhang, J.; Zhu, Y. Heterogeneous photoresponse of individual grain in all-inorganic perovskite solar cells. *Appl. Phys. Lett.* **2020**, *117*, 083902–083906. [[CrossRef](#)]
5. NREL. Best Research-Cell Efficiency Chart. 2022. Available online: <https://www.nrel.gov/pv/cell-efficiency.html> (accessed on 25 September 2022).
6. Duan, J.; Zhao, Y.; Yang, X.; Wang, Y.; He, B.; Tang, Q. Lanthanide Ions Doped CsPbBr₃ Halides for HTM-Free 10.14%-Efficiency Inorganic Perovskite Solar Cell with an Ultrahigh Open-Circuit Voltage of 1.594 V. *Adv. Energy Mater.* **2018**, *8*, 1–9. [[CrossRef](#)]
7. Ren, Y.; Zhang, N.; Arain, Z.; Mateen, M.; Chen, J.; Sun, Y.; Li, Z. Polymer-induced lattice expansion leads to all-inorganic CsPbBr₃ perovskite solar cells with reduced trap density. *J. Power Sources* **2020**, *475*, 228676. [[CrossRef](#)]
8. Liu, X.; Liu, Z.; Tan, X.; Ye, H.; Sun, B.; Xi, S.; Shi, T.; Tang, Z.; Liao, G. Novel antisolvent-washing strategy for highly efficient carbon-based planar CsPbBr₃ perovskite solar cells. *J. Power Sources* **2019**, *439*, 227092. [[CrossRef](#)]
9. Liu, J.; Zhu, L.; Xiang, S.; Wei, Y.; Xie, M.; Liu, H.; Li, W.; Chen, H. Growing high-quality CsPbBr₃ by using porous CsPb₂Br₅ as an intermediate: A promising light absorber in carbon-based perovskite solar cells. *Sustain. Energy Fuels* **2019**, *3*, 184–194. [[CrossRef](#)]
10. Xu, H.; Duan, J.; Zhao, Y.; Jiao, Z.; He, B.; Tang, Q. 9.13%-Efficiency and stable inorganic CsPbBr₃ solar cells. Lead-free CsSnBr₃-xI_x quantum dots promote charge extraction. *J. Power Sources* **2018**, *399*, 76–82. [[CrossRef](#)]

11. Tong, G.; Chen, T.; Li, H.; Qiu, L.; Liu, Z.; Dang, Y.; Song, W.; Ono, L.K.; Jiang, Y.; Qi, Y. Phase transition induced recrystallization and low surface potential barrier leading to 10.91%-efficient CsPbBr₃ perovskite solar cells. *Nano Energy* **2019**, *65*, 104015. [[CrossRef](#)]
12. Yuan, H.; Zhao, Y.; Duan, J.; Wang, Y.; Yang, X.; Tang, Q. All-inorganic CsPbBr₃ perovskite solar cell with 10.26% efficiency by spectra engineering. *J. Mater. Chem. A* **2018**, *6*, 24324–24329. [[CrossRef](#)]
13. Duan, J.; Zhao, Y.; He, B.; Tang, Q. High-Purity Inorganic Perovskite Films for Solar Cells with 9.72 % Efficiency. *Angew. Chem.* **2018**, *130*, 3849–3853. [[CrossRef](#)]
14. Wang, K.; Jin, Z.; Liang, L.; Bian, H.; Bai, D.; Wang, H.; Zhang, J.; Wang, Q.; Liu, S. All-inorganic cesium lead iodide perovskite solar cells with stabilized efficiency beyond 15%. *Nat. Commun.* **2018**, *9*, 1–8. [[CrossRef](#)]
15. Zhu, J.; Tang, M.; He, B.; Shen, K.; Zhang, W.; Sun, X.; Sun, M.; Chen, H.; Duan, Y.; Tang, Q. Ultraviolet filtration and defect passivation for efficient and photostable CsPbBr₃ perovskite solar cells by interface engineering with ultraviolet absorber. *Chem. Eng. J.* **2020**, *404*, 126548. [[CrossRef](#)]
16. Jiang, J.; Jin, Z.; Gao, F.; Sun, J.; Wang, Q.; Liu, S. CsPbCl₃-Driven Low-Trap-Density Perovskite Grain Growth for >20% Solar Cell Efficiency. *Adv. Sci.* **2018**, *5*, 1800474. [[CrossRef](#)]
17. Wang, Z.; Lin, Q.; Chmiel, F.P.; Sakai, N.; Herz, L.; Snaith, H. Efficient ambient-air-stable solar cells with 2D–3D heterostructured butylammonium-caesium-formamidinium lead halide perovskites. *Nat. Energy* **2017**, *2*, 17135. [[CrossRef](#)]
18. Liu, M.; Dahlström, S.; Ahläng, C.; Wilken, S.; Degterev, A.; Matuhina, A.; Hadadian, M.; Markkanen, M.; Aitola, K.; Kamppinen, A.; et al. Beyond hydrophobicity: How F4-TCNQ doping of the hole transport material improves stability of mesoporous triple-cation perovskite solar cells. *J. Mater. Chem. A* **2022**, *10*, 11721–11731. [[CrossRef](#)]
19. Saliba, M.; Stolterfoht, M.; Wolff, C.M.; Neher, D.; Abate, A. Measuring Aging Stability of Perovskite Solar Cells. *Joule* **2018**, *2*, 1019–1024. [[CrossRef](#)]
20. Zhou, Q.; Duan, J.; Yang, X.; Duan, Y.; Tang, Q. Interfacial Strain Release from the WS₂/CsPbBr₃ van der Waals Heterostructure for 1.7 V Voltage All-Inorganic Perovskite Solar Cells. *Angew. Chem. Int. Ed.* **2020**, *59*, 21997–22001. [[CrossRef](#)]
21. Li, N.; Zhu, Z.; Chueh, C.-C.; Liu, H.; Peng, B.; Petrone, A.; Li, X.; Wang, L.; Jen, A.K.-Y. Mixed Cation FA_xPEA_{1-x}PbI₃ with Enhanced Phase and Ambient Stability toward High-Performance Perovskite Solar Cells. *Adv. Energy Mater.* **2016**, *7*, 1–9. [[CrossRef](#)]
22. Zhang, F.; Kim, D.H.; Lu, H.; Park, J.-S.; Larson, B.W.; Hu, J.; Gao, L.; Xiao, C.; Reid, O.G.; Chen, X.; et al. Enhanced Charge Transport in 2D Perovskites via Fluorination of Organic Cation. *J. Am. Chem. Soc.* **2019**, *141*, 5972–5979. [[CrossRef](#)] [[PubMed](#)]
23. Jiang, Q.; Zhao, Y.; Zhang, X.; Yang, X.; Chen, Y.; Chu, Z.; Ye, Q.; Li, X.; Yin, Z.; You, J. Surface passivation of perovskite film for efficient solar cells. *Nat. Photon.* **2019**, *13*, 460–466. [[CrossRef](#)]
24. Wu, J.; Dong, J.-J.; Chen, S.-X.; Hao, H.-Y.; Xing, J.; Liu, H. Fabrication of Efficient Organic-Inorganic Perovskite Solar Cells in Ambient Air. *Nanoscale Res. Lett.* **2018**, *13*, 293. [[CrossRef](#)] [[PubMed](#)]
25. Yan, J.; Hou, S.; Li, X.; Dong, J.; Zou, L.; Yang, M.; Xing, J.; Liu, H.; Hao, H. Preparation of highly efficient and stable CsPbBr₃ perovskite solar cells based on an anti-solvent rinsing strategy. *Sol. Energy Mater. Sol. Cells* **2022**, *234*, 111420–111428. [[CrossRef](#)]
26. Fu, W.; Liu, H.; Shi, X.; Zuo, L.; Li, X.; Jen, A.K. Tailoring the Functionality of Organic Spacer Cations for Efficient and Stable Quasi-2D Perovskite Solar Cells. *Adv. Funct. Mater.* **2019**, *29*, 1–8. [[CrossRef](#)]
27. Yun, Y.; Wang, F.; Huang, H.; Fang, Y.; Liu, S.; Huang, W.; Cheng, Z.; Liu, Y.; Cao, Y.; Gao, M.; et al. A Nontoxic Bifunctional (Anti)Solvent as Digestive-Ripening Agent for High-Performance Perovskite Solar Cells. *Adv. Mater.* **2020**, *32*, e1907123. [[CrossRef](#)] [[PubMed](#)]
28. Lee, K.; Kim, J.; Yu, H.; Lee, J.W.; Yoon, C.-M.; Kim, S.K.; Jang, J. A highly stable and efficient carbon electrode-based perovskite solar cell achieved via interfacial growth of 2D PEA₂PbI₄ perovskite. *J. Mater. Chem. A* **2018**, *6*, 24560–24568. [[CrossRef](#)]
29. Canil, L.; Salunke, J.; Wang, Q.; Liu, M.; Köbler, H.; Flatken, M.; Gregori, L.; Meggiolaro, D.; Ricciarelli, D.; De Angelis, F.; et al. Halogen-Bonded Hole-Transport Material Suppresses Charge Recombination and Enhances Stability of Perovskite Solar Cells. *Adv. Energy Mater.* **2021**, *11*, 2101553. [[CrossRef](#)]